analytical chemistry

pubs.acs.org/ac Article

D-π-A Dual-Mode Probe Design for the Detection of nM-Level Typical Oxidants

Xinyi Yang,[‖] Zhenzhen Cai,[‖] Dezhong Li, Da Lei, Yushu Li, Guangfa Wang, Jun Zhang,* and Xincun Dou*

Cite This: *Anal. Chem.* 2022, 94, 9184−9192 Read Online

ACCESS | Metrics & More | Article Recommendations | Supporting Information

ABSTRACT: Although a set of functional molecules with the D-π-A structure has been explored as optical probes for the detection of target analytes, it remains a great challenge to elaborately design a single probe for distinguishing different analytes by their intrinsic oxidation or reduction capabilities and thus to generate distinct optical responses. Here, a unique TCF-based probe (DMA-CN) containing two unsaturated double bonds in the π-conjugation bridge and TCF with different reaction activities that could be cut off by $KMnO_4$ and NaClO in varying degrees was developed, causing remarkably distinguishable responses for both fluorescence and colorimetric channels to discriminate $KMnO_4$ and NaClO from each other. The fluorescence and colorimetric limits of detection (LODs) of the proposed DMA-CN toward $KMnO_4$ were calculated as 60 and 91 nM, respectively, while those for NaClO were 13.3 and 214 nM, and all the optical signal change can be observed within 1 s with good specificity. Based on the proposed probe design strategy, a well-fabricated test strip was proven to be promising for the rapid, in-field detection and risk management. We expect that the present probe design methodology would provide a powerful strategy for efficient probe exploration, especially for discriminating the substances with similar oxidizing properties.

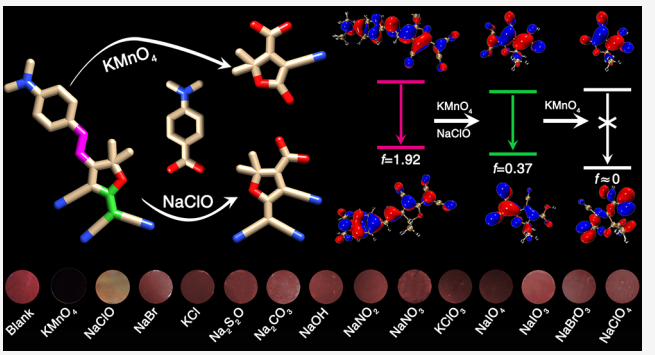

Optical probes for sensing purposes usually contain an active recognition center coupled with an intense chromophore or fluorophore to interact strongly with the target analyte.[1−3] Among them, organic optical probes,[4−7] which possess the advantages of adjustable structures, various functional groups, high luminescence efficiency, fast response, and specific recognition sites, have attracted considerable attention and serve as an effective tool in ion analysis,[8−10] explosive detection,[1,11] gas sensing,[12,13] etc. When both electron-donating and electron-withdrawing groups are conjugated into one π-electron system, a typical electron donor−π conjugation bridge−electron acceptor (D-π-A) molecule can be generated.[14] The donor moiety is usually amino, pyrene, carbazole, indoline etc., while the π-conjugation bridge is composed of thiophene, furan, benzene units, etc., and the acceptor is constituted by malononitrile, indandione, etc.[15] Some functional molecules with the D-π-A structure have been widely applied in intensity-dependent fluorimetry, strong solvatochromism, nonlinear optical materials, organic photovoltaics, and fluorescence imaging.[16−18] To date, most of the reported optical probes were designed by changing the electron-donating ability,[19] the electron-withdrawing ability,[20] or the π-conjugation degree[21,22] of the chromophores or fluorophores during interacting with the analyte. A series of studies have focused on the regulation of the probe structure to enhance the detection performance toward a single target, typically, for which the oxidation or reduction capability of the analyte was employed to interact with the π-conjugation bridge, resulting in a specific optical signal change. However, whether this signal change could be designed to distinguish different analytes depending on their intrinsic oxidation or reduction capability, thus generating distinct optical responses, remains unknown.

Typical oxidants, such as potassium permanganate ($KMnO_4$) and sodium hypochlorite (NaClO), are extensively used in manufacturing chemicals due to their strong oxidative property. Nevertheless, the excessive emissions of $KMnO_4$ and NaClO could result in environmental pollution, and excessive intake can affect the ordered functioning of biological systems.[23−26] Therefore, rapid, highly sensitive, and visualized identification toward these typical oxidants is of great significance for public health and environmental monitoring.

Received: April 29, 2022
Accepted: June 3, 2022
Published: June 17, 2022

https://doi.org/10.1021/acs.analchem.2c01894
Anal. Chem. 2022, 94, 9184−9192

It is well-known that the unsaturated double bond has been employed as the recognition site for detecting oxidants by breaking it.[17,24,27] It is also a common sense that the oxidation capability of $KMnO_4$ and NaClO is different and both of them can oxidize the unsaturated double bond. Therefore, a probe molecule elaborately designed by taking full advantage of the different reaction activities of the unsaturated double bonds to specifically react with $KMnO_4$ and NaClO is a preferable but challenging option.

To this end, we designed a D-π-A probe ((*E*)-2-(3-cyano-4-(4-(dimethylamino)styryl)-5,5-dimethylfuran-2(5*H*)-ylidene)-malononitrile, DMA-CN) containing two unsaturated double bonds with different reaction activities for discriminating $KMnO_4$ and NaClO. The resulting fluorescence−colorimetric dual-mode responses could be attributed to the successful creation of these two unsaturated double bonds, in which one originated intrinsically in 2-(3-cyano-4,5,5-trimethylfuran-2(5*H*)-ylidene) malononitrile (TCF) and the other was from the π-conjugation bridge formed through the Claisen−Schmidt coupling reaction between TCF and 4-dimethylaminobenzaldehyde. Due to the different oxidizing properties of $KMnO_4$ and NaClO, the unsaturated double bonds in the π-conjugation bridge and TCF can be cut off in varying degrees within 1 s, causing different responses in the fluorescence and colorimetric channels. In addition, it has been proven that 12 types of oxidants and common anions or cations have a negligible influence on the detection specificity. The proposed probe design strategy was further demonstrated to be applicable for the rapid, in-field analysis of $KMnO_4$ and NaClO by incorporating it into a nanofibrous film sensor.

EXPERIMENTAL SECTION

Materials and Characterization. Unless otherwise noted, all reagents and materials were obtained from commercial sources and used without further purification. Poly(methyl methacrylate) (PMMA) was purchased from Sigma-Aldrich Trading Co., Ltd. 4-Dimethylaminobenzaldehyde, sodium ethanol, 3-hydroxy-3-methyl-2-butanone, malononitrile, and poly(vinyl alcohol) (PVA, MW 60,000) were purchased from Aladdin Chemical Reagent Ltd., and all the organic solvents such as dimethyl sulfoxide (DMSO) and tetrahydrofuran (THF) and inorganic salts were bought from Sinopharm Chemical Reagent Ltd. Solvents used for synthesis and optical property characterization were analytical grade and chromatographic grade, respectively.

Using tetramethylsilane (TMS) as the internal standard, ^1H NMR and ^{13}C NMR spectra were measured on a high-resolution 400 MHz superconducting NMR spectrometer (Varian). Mass spectra of fluorescent probes and products were determined with a Q Exactive-type four-stage rod-Orbitrap high-resolution mass spectrometer (HRMS, UHPLC-Q-Orbitrap-HRMS, Thermo Fisher Scientific). UV−vis absorption spectra were measured on a UV-3900 UV−vis spectrophotometer (Hitachi, Japan), and fluorescence spectra (Edinburgh Instruments, U.K.) were collected on an Edinburgh FLS1000 fluorescence spectrophotometer. Fourier transform infrared (FT-IR) spectra were obtained using a Frontier thermogravimetric infrared analysis system (PierkinElmer, Japan). The morphology and structure of nanofibrous films were characterized using a field-emission scanning electron microscope (FE-SEM JEOL JSM-7610F Plus, Japan) by operating at 4.0−6.0 kV. The contact angle was determined with a GX-28 rapid specific surface area and void analyzer. Dark-field images were collected on a Nikon Ti-E inverted fluorescence microscope, and the optical images were obtained using Apple 12. *R*, *G*, and *B* values were extracted using Adobe Photoshop software.

Computational Details. All ground-state geometric structures (S0) were fully optimized using the PBE0[28] exchange−correlation functional with Grimme's DFT-D3-(BJ)[29] empirical dispersion correction, abbreviated as PBE0-D3(BJ). The 6-311G(d,p)[30] basis set was adapted for all atoms. The structures of the lowest singlet excited S1 state were optimized based on time-dependent density functional theory (TD-DFT)[31] at the PBE0-D3(BJ)/6-311G(d,p) level to evaluate the vertical emission energies since the PBE0 functional is found to provide a good balance between the local excited (LE) and intramolecular charge transfer (ICT) states, with an average absolute error of ca. 0.14 eV for the low-lying excited states of conjugated organic compounds.[32] A further frequency calculation at the same level of theory was also carried out with the optimized geometries to ensure that the located stationary points do not have any imaginary frequency. Then, the vertical absorption energies were determined based on the S0 structure using TD-DFT at the same level, and only the first 40 singlet excited states are taken into account. The vertical emission energies were calculated as the vertical de-excitation on the basis of the lowest excited-state optimized structure S1. The first three singlet−singlet electronic transitions (S1 → S0) were computed based on the TD-DFT method. Still, all the computing tasks are simulated in DMSO. Throughout, solvent effects have been modeled using the linear response polarizable continuum method (PCM)[33] implemented in the Gaussian 09[34] code. The noncovalent interaction analysis using the independent gradient model (IGM)[35] was applied to investigate the hydrogen bond interaction between the PVA unit and the probe. The above-mentioned wave function analysis was produced using the Multiwfn[36] program and VMD[37] software.

RESULTS AND DISCUSSION

Design and Synthesis of the TCF-Based D-π-A Dual-Responsive Probe. It is considered that the optical properties of the DMA-CN probe, including the molar absorption coefficient and a shift in the fluorescence spectrum, could be well modulated by combining 4-dimethylaminobenzaldehyde as a donor and TCF as an acceptor (Figures 1a and S1−S5 andScheme S1). If an analyte can interact with them, the degree of the π-conjugation system, the fluorescent emission wavelength, and (or) the fluorescence quantum yield should be changed. It should be noted that although DMA-CN has been synthesized previously and used in a variety of fields,[38−41] no one has focused on how to utilize the activity difference of the unsaturated double bonds to develop functional probes.

Both the unsaturated double bonds in the π-conjugation bridge and TCF would be cut off by $KMnO_4$ due to its strong oxidizing capability (Figure 1b), subsequently generating the products including 4-(dimethylamino)benzoic acid (D-COOH), 4-cyano-2,2-dimethyl-5-oxo-2,5-dihydrofuran-3-carboxylic acid (A-CO), and 4-cyano-5-(dicyanomethylene)-2,2-dimethyl-2,5-dihydrofuran-3-carboxylic acid (A-CN). The structure of these products could be firmly evidenced by the disappearance of the peak at m/z 331.15 corresponding to DMA-CN and the appearance of the peaks at m/z 166.81, 181.09, and 229.12 in the HRMS data (Figure S6), whereas

https://doi.org/10.1021/acs.analchem.2c01894
Anal. Chem. 2022, 94, 9184−9192

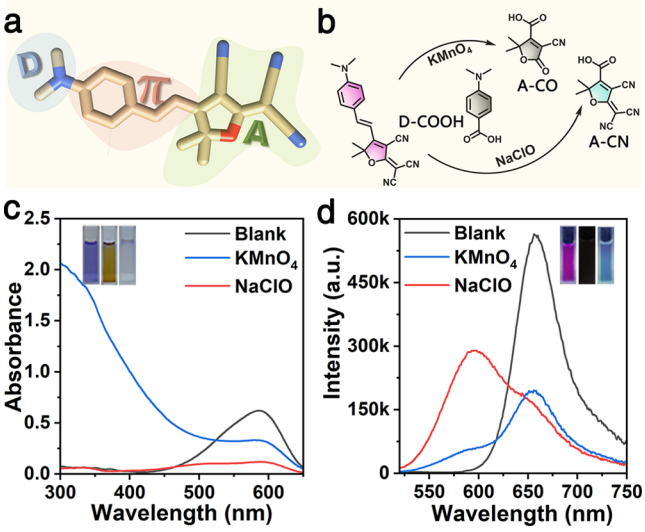

Figure 1. (a) Schematic illustration of the design of the DMA-CN probe with the D-π-A structure; (b) proposed detection mechanism of DMA-CN toward $KMnO_4$ and NaClO; (c) UV−vis absorption; and (d) fluorescence emission spectra of DMA-CN (in THF/DMSO/H_2O with a volume ratio of 5:25:1, 8 μM) toward $KMnO_4$ and NaClO (0.25 mM).

only the double bond in the π-conjugation bridge could be cut off in the presence of NaClO due to its relatively weak oxidizing property. This was confirmed by the reaction products D-COOH and A-CN with the new HRMS peaks located at m/z 166.07 and 229.22, respectively (Figure S7). In addition, the ^1H and ^{13}C NMR spectra of A-CN and A-CO (Figures S8−S11) can further clarify the structure of the reaction product of DMA-CN toward $KMnO_4$ and NaClO, respectively.

To gain a high sensing performance, a mixture of THF, DMSO, and H_2O with a volume ratio of 5:25:1 was determined as the reaction solvent. It should be noted that this ratio was systematically optimized from four aspects: (i) the most pronounced blank emission, (ii) the environmental toxicity brought by THF (Figure S12), (iii) the high boiling point of DMSO to inhibit the solvent volatilization and to ensure the concentration consistency (Figure S13), and (iv) the dissolving function of the target analytes favored by introducing a little amount of water (Figure S14). Both additions of $KMnO_4$ and NaClO could lead to a decrease of the characteristic absorption peak centered at 587 nm to different extents along with an obvious fading of the blue color of DMA-CN, further proving the effective breaking of the double bond in the π-conjugation bridge. The resulting yellowish color of the solution after the addition of $KMnO_4$ could be ascribed to the reductive product of $KMnO_4$, which was accompanied with a new maximum absorption around 400 nm (Figure 1c) and the quenching of the purple emission located at 657 nm (Figure 1d), while the emergence of a steel-blue emission at 595 nm after detecting NaClO represents the characteristic fluorescence of A-CN. Although the incomplete reaction residue of A-CN could also emit very weak steel-blue fluorescence while detecting $KMnO_4$, it is heavily shadowed by the dark background and will not result in any influence on the discrimination of $KMnO_4$ from NaClO by the distinct colorimetric or fluorescence response.

The S1 → S0 emission hole−electron analysis[42] of DMA-CN shows that although there is an overlap of distributions of

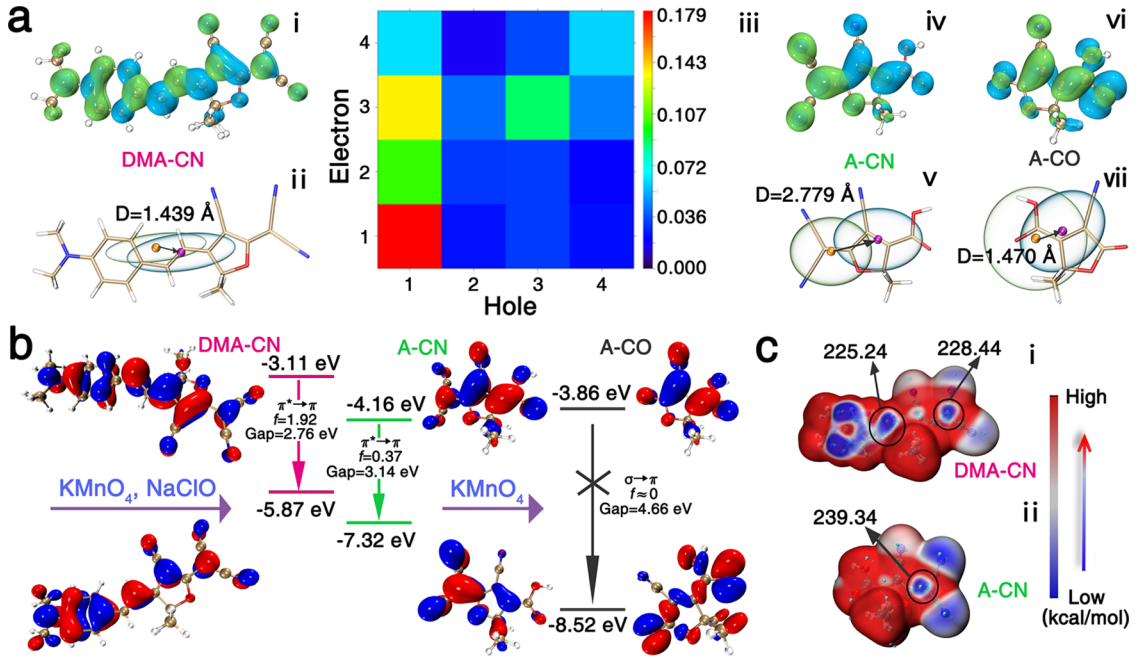

Figure 2. (a) Hole−electron analysis of (i) hole and electron distributions of the DMA-CN: S1 → S0 emission (isovalue = 0.001) with the green and blue regions denoting the hole and electron distributions, respectively, (ii) C_{hole}/C_{ele} map smoothly transformed from hole and electron distributions, the centroids of C_{hole}/C_{ele} were marked by the orange and purple spheres with the charge transfer distance represented as D, (iii) fragment transition density matrix map corresponding to the index of four self-defined fragments, (iv) hole−electron analysis, and (v) C_{hole}/C_{ele} diagram of A-CN, (vi) hole−electron analysis, and (vii) C_{hole}/C_{ele} diagram of A-CO; (b) dominant contributions of MO transitions in DMA-CN and the reaction products: S1 → S0 emission (isovalue = 0.02), red and blue regions denote the positive and negative orbital phases, respectively, the numbers denote the energy of the orbital (in eV); and (c) average local ionization energy (ALIE) of (i) DMA-CN and (ii) A-CN.

https://doi.org/10.1021/acs.analchem.2c01894
Anal. Chem. 2022, 94, 9184−9192

holes and electrons, represented in blue and green areas, a distinct hole distribution near dimethylamine and a dominant electron distribution near TCF still exist (Figure 2a-i). The distance from the center of the hole distribution to the center of the electron distribution yields an electron excitation of 1.439 Å, which is the approximate length of one C−C bond, with a t-index value of −2.21 (Table S1), which could be attributed to the local excitation (LE) mechanism (Figure 2a-ii). By dividing the DMA-CN probe molecule into four fragments (Figure S15) and employing the fragment charge transfer matrix, the heat map with different colors corresponding to the density of holes and electrons in different fragments could be obtained (Figure 2a-iii). From the perspective of the horizontal coordinate, which represents the hole distribution, the maximum density is located in fragments 1 and 3, denoted by red and light green regions, respectively, indicating that the hole distribution is mainly concentrated in these two fragments. In contrast, it could be seen from the vertical coordinate that there are relatively dispersed electron distributions in fragments 1, 2, and 3 with the maximum densities displayed in red, green, and yellow, respectively. This demonstrates that although a small portion of the excited electrons could transfer from fragment 1 to 2, the overall transfer is strictly limited in the restricted areas with both hole and electron distributions decentralized in fragments 1 and 3, respectively, which further verifies that LE is the dominant excitation contributing to the S1 → S0 emission of DMA-CN. It is found that there is an obvious separation of the hole/electron distributions in A-CN and a considerably large D index of 2.779 Å, which is longer than two times the C−C bond length (Figure 2a-iv,2a-v), whereas the hole/electron distributions seriously overlap and disperse all over the whole A-CO molecule with a small D index (1.470 Å), close to that of DMA-CN (Table S1). Thus, it is clearly indicated that the S1 → S0 emission of A-CN and A-CO could be classified into ICT and LE, respectively (Figures 2a-vi,2a-vii).

Based on the electron excitation analysis, the emission of the DMA-CN probe is generated from the $\pi^* \rightarrow \pi$ emission of the LUMO to the HOMO (S1 → S0) with a HOMO/LUMO gap of 2.76 eV and results in a new fluorescence peak located at 568 nm with a high oscillator strength (f = 1.92) (Figure 2b and Table S1). After the detection of the oxidants, the A-CN product shows a fluorescence emission with a larger HOMO/LUMO gap of 3.14 eV and a lower f (0.37). On the contrary, the emission of the A-CO product shows a different orbital characteristic, which could be ascribed to the $\pi^* \rightarrow \sigma$, causing a much larger HOMO/LUMO gap of 4.66 eV and a forbidden transition of fluorescence emission with the f approaching 0.

Furthermore, the average local ionization energy (ALIE)[43] analysis is preformed to determine the binding affinity of the different sites in DMA-CN and A-CN by marking the high-electron energy area in blue; this implies more possibility of further nucleophilic reaction taking place (Figure 2c). Although there are a set of blue areas located at the benzene ring and −CN groups, they can hardly react with oxidants. Meanwhile, there are two obvious blue regions concentrated at the unsaturated double bonds in the π-conjugation bridge and TCF with the ALIE values of 225.24 and 228.44 kcal/mol, respectively (Figure 2c-i), implying that the unsaturated double bond in the π-conjugation bridge is more active and easier to be oxidized. In addition, the lowest ALIE in A-CN is located at the unsaturated double bond with a value of 239.34 kcal/mol (Figure 2c-ii), demonstrating the feasibility of the preferential breaking of the double bond in the π-conjugation bridge and the further breaking of the double bond in the produced A-CN. Thus, it is apparently verified that the two unsaturated double bonds with different reactivities in DMA-CN can be sequentially used for detecting and discriminating $KMnO_4$ and NaClO depending on their different oxidative activities upon fluorescence emission difference.

Colorimetric Detection and Discrimination of $KMnO_4$ and NaClO. The UV−vis absorption spectra and the time-dependent optical images of DMA-CN toward $KMnO_4$ and NaClO were first evaluated. It is apparent that the absorption peak at 587 nm of DMA-CN gradually decreases along with the addition of the increasing $KMnO_4$ (0−250 μM), and a broad absorption in the range from 300 to 450 nm emerges with an elevated absorption (Figure 3a). Meanwhile, a color change from blue to yellowish occurs, which could be attributed to the color of the reduction product of $KMnO_4$, which could be applied for judging the existence of $KMnO_4$. In terms of the detection toward NaClO, the intensity of the characteristic absorption peak at 587 nm of DMA-CN keeps decreasing with a gradual color change from blue to colorless

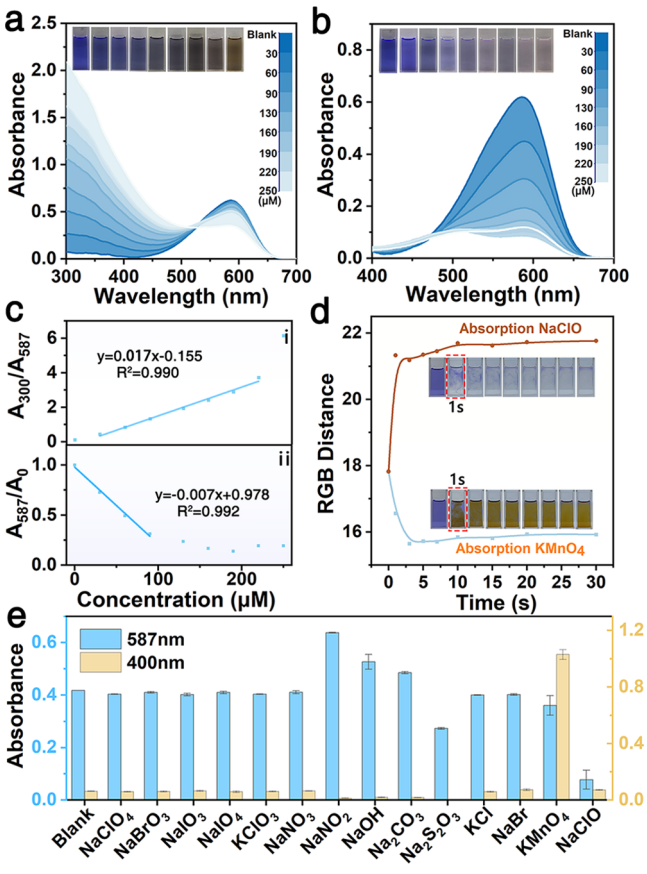

Figure 3. Colorimetric performances of DMA-CN toward $KMnO_4$ and NaClO. UV−vis absorption spectra obtained in response to different concentrations of (a) $KMnO_4$ and (b) NaClO and the corresponding images; (c) absorption intensity ratio (A_{300}/A_{587}) as a function of $KMnO_4$ concentration and (ii) absorption intensity ratio (A_{587}/A_0) of the peak at 587 nm before (A_0) and after (A_{587}) interacting with different concentrations of NaClO; (d) optical images of time-dependent colorimetric response and the corresponding RGB distances of DMA-CN upon the addition of $KMnO_4$ and NaClO; (e) and intensity comparison of the colorimetric specificity obtained for DMA-CN in response to various analytes (0.25 mM).

https://doi.org/10.1021/acs.analchem.2c01894
Anal. Chem. 2022, 94, 9184−9192

(Figure 3b) when the NaClO concentration varies from 0 to 250 μM. Furthermore, the ratio of the absorbance (I_{300}/I_{587}) increases linearly in the presence of $KMnO_4$ with an ascending concentration from 0 to 220 μM (Figure 3c-i). For the detection of NaClO, the intensity of the absorption at 587 nm was linearly proportional to the NaClO concentration in the range of 0−90 μM (Figure 3c-ii). The colorimetric LODs, defined as $3\sigma/k$, where σ is the standard deviation of the blank solution with a value of 0.0005 and k is the slope of the linear fitting curve, were then calculated as 91 and 214 nM for $KMnO_4$ and NaClO, respectively. Furthermore, the concentrations of the product A-CO and the analyte $KMnO_4$ show a great linear relevance, also strongly suggesting that the concentration of A-CO is dependent on the added amount of $KMnO_4$ (Figure S16).

The time-dependent colorimetric images were recorded to evaluate the response time and stability of the probe (Figure 3d). It can be observed that the colorimetric signal response can be observed within 1 s for both $KMnO_4$ and NaClO. Upon the analysis of the corresponding averaged RGB distance variation, the time duration for the reaction to reach a steady state could be defined as short as 3 s. To confirm the detection specificity of DMA-CN toward $KMnO_4$ and NaClO, more than 10 substances consisting of oxidants and common anions and cations were selected as the potential interferents. It can be observed that compared with the notable decrease caused by $KMnO_4$ and NaClO, the addition of these interferents (0.25 mM) did not result in an obvious change in the UV−vis absorption spectra (Figures 3e and S17). It should be noted that the oxidants, including $NaNO_3$, $KClO_3$, $NaIO_4$, $NaIO_3$, $NaBrO_4$, and $NaClO_4$, which also have strong oxidative capability, did not cause the breaking of any unsaturated double bonds equipped within the probe, demonstrating the unique priority of the designed DMA-CN probe toward $KMnO_4$ and NaClO.

Fluorescence Detection and Discrimination of $KMnO_4$ and NaClO. The fluorescence sensitivity of the DMA-CN toward $KMnO_4$ and NaClO was evaluated in the concentration range of 0−250 μM. The fluorescence intensity of the emission centered at 657 nm decreases gradually with the increased $KMnO_4$, and a weak fluorescence emission centered at 595 nm appears when the $KMnO_4$ concentration reaches 250 μM, accompanied with a sharp decrease of the purple emission followed by the complete quenching (Figure 4a). Meanwhile, with the increased NaClO, the emission of DMA-CN at 657 nm gradually decreased, along with the emergence of an emission peak at 595 nm once the NaClO concentration exceeds 60 μM (Figure 4b). At the same time, the purple fluorescence fades quickly and changes to steel blue when the NaClO concentration reaches 90 μM because of the coexistence of DMA-CN with purple fluorescence and A-CN with yellow orange fluorescence (Figure S18).

The fluorescence intensity shows a linear optical behavior with respect to the increasing $KMnO_4$ concentration in the range of 30−190 μM. Furthermore, the LOD for DMA-CN toward $KMnO_4$ is calculated as 60 nM according to $3\sigma/k$ with a σ of 0.00004 (Figure 4c-i). By comparing this LOD with that in previously reported studies (Table S2), the higher sensitivity of the DMA-CN probe is undoubtedly confirmed, and the superiority of the proposed sensing strategy is ambitiously imposed. For the NaClO detection, it is found that the fluorescence intensity ratio (I_{595}/I_{657}) was linearly proportional to the NaClO concentration in the range of 0−160 μM (Figure 4c-ii). Moreover, the quantitative information of oxidation products could be supported with the working curve of A-CN, which was established based on the relevance between the analyte concentration and the A-CN/A-CO concentration, indicating that the concentration-dependent relevance of the analyte and product is consistent with the proposed oxidation mechanism (Figures S19 and S20). In addition, the LOD was determined as 13.3 nM, which is superior than that of most of the reported NaClO probes with a LOD ranging from 3.17 to 170 nM (Table S3). The fluorescence response time of DMA-CN toward $KMnO_4$ and NaClO is similar to that in the colorimetric mode, with a visible discerning time of 1 s and a time duration of 3 s to reach the steady state (Figure 4d). Furthermore, various interferents fail to exhibit a similar fluorescence response toward $KMnO_4$ and NaClO, indicating the desirable specificity of the probe toward the targets (Figures 4e and S21). It is worthy to note that the LODs of the fluorescent mode are 1.5 ($KMnO_4$) and 16.1 (NaClO) times lower than those from the colorimetric mode, strongly suggesting a much more superior sensitivity of the fluorescent mode with equivalently good specificity and rapid response within 1 s. Hence, the fluorescence characteristics of the probe are much more prominent for the in-field applications.

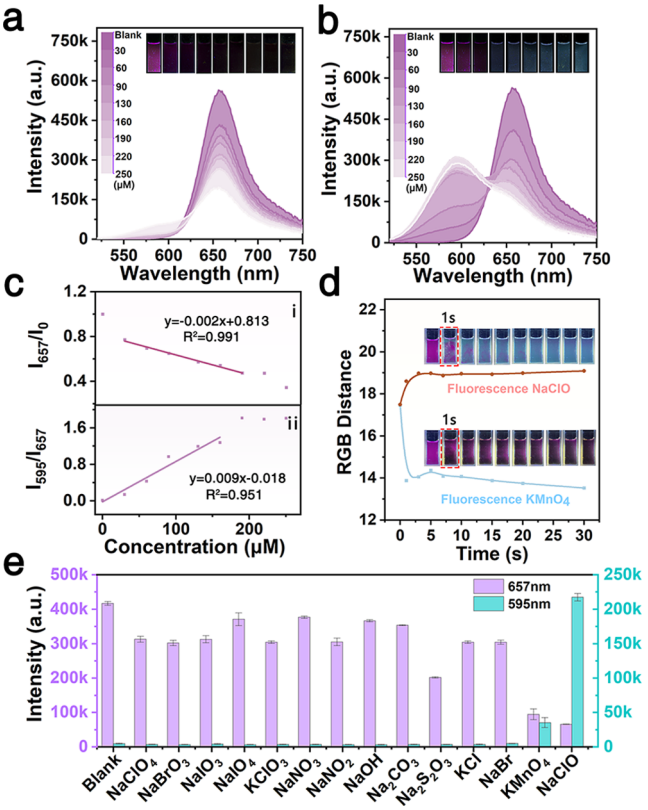

Figure 4. Fluorescence performances of DMA-CN toward $KMnO_4$ and NaClO. Fluorescence emission spectra obtained in response to different concentrations of (a) $KMnO_4$ and (b) NaClO; (c) (i) intensity ratio (I_{657}/I_0) of the peak at 657 nm before (I_0) and after (I_{657}) interacting with different concentrations of $KMnO_4$ and (ii) emission intensity ratio (I_{595}/I_{657}) as a function of NaClO concentration; (d) optical images of the time-dependent fluorescent response and the corresponding RGB distances of DMA-CN for the detection of $KMnO_4$ and NaClO, respectively; and (e) intensity comparison of the fluorescent specificity obtained for DMA-CN in response to various analytes (0.25 mM).

https://doi.org/10.1021/acs.analchem.2c01894
Anal. Chem. 2022, 94, 9184−9192

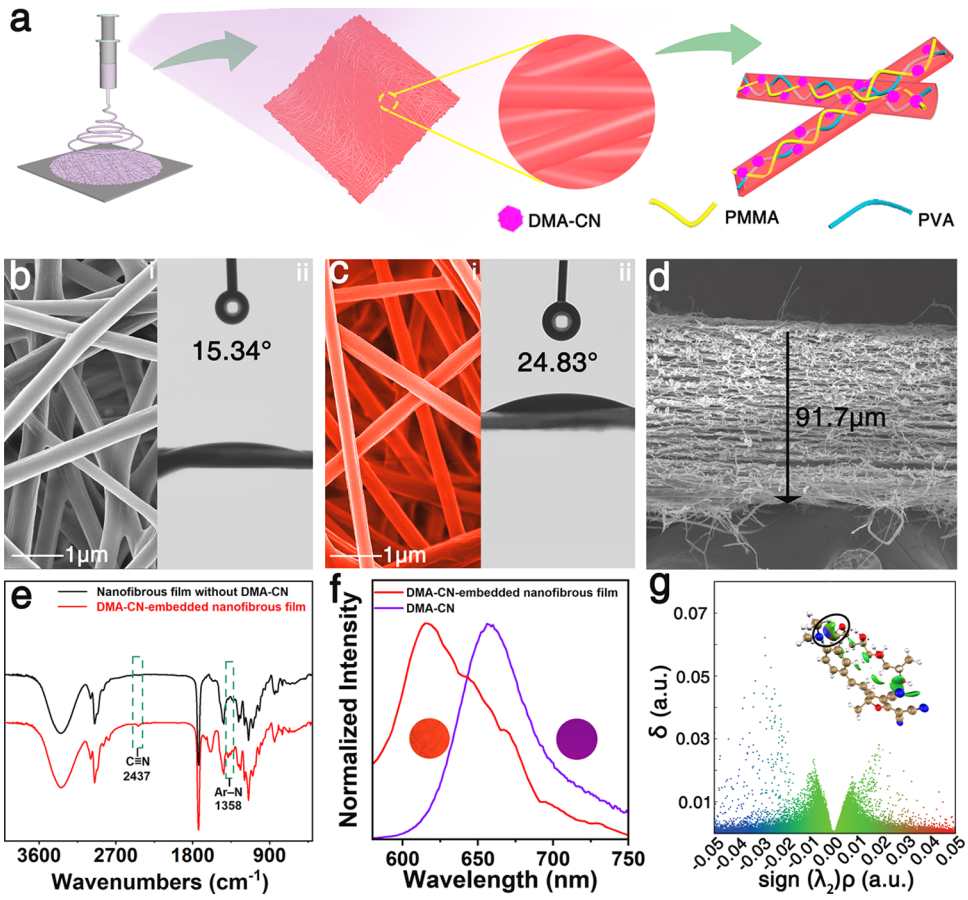

Figure 5. (a) Schematic illustration of the fabrication process of the DMA-CN-embedded nanofibrous film; (b) (i) SEM and (ii) contact angle images of the nanofibrous film without DMA-CN; (c) (i) SEM and (ii) contact angle images of the DMA-CN-embedded nanofibrous film; (d) SEM characterization of the cross section of the DMA-CN-embedded nanofibrous film; (e) FT-IR spectra of the nanofibrous films before and after embedding DMA-CN; (f) normalized fluorescence emission spectra and the corresponding optical images of DMA-CN and DMA-CN-embedded nanofibrous film in dark field; and (g) scatter graph and isosurface (value = 0.01 a.u.) of the noncovalent interactions between the PVA unit and DMA-CN probe.

Fabrication of the DMA-CN-Embedded Nanofibrous Film. To develop a simple, cheap, fast, and reliable sensor toward $KMnO_4$ and NaClO detection, DMA-CN-embedded nanofibers were fabricated by adding the DMA-CN probe to the mixture solution of poly(vinyl alcohol) (PVA) and poly(methyl methacrylate) (PMMA) for the electrospinning (Figure 5a). To obtain a nanofibrous film that can be reliably applied for more efficient detection of $KMnO_4$ or NaClO, the ratio of PMMA and PVA should be first optimized, which is responsible for the film wettability. It is found that the hydrophilicity of the nanofibrous film could be improved with the increased content of PVA, and when the volume ratio of PVA to PMMA reaches 7:3, the contact angle of the film could be obtained desirably with a value of 15.34°, regardless of the morphology change of the film (Figures 5b and S22 and S23). By embedding the DMA-CN probe into the nanofibrous film, the contact angle was increased a little to 24.83° due to the hydrophobicity of DMA-CN while without the morphology change (Figure 5c). Although this contact angle shows a little increase, it is still favorable enough for the aqueous analyte solution easily penetrating inside the film.

In addition, the thickness of the DMA-CN-embedded nanofibrous film was approximately 91.7 μm, which would endow enough pore space for the reaction and a good mechanical strength for a film sensor being practically used (Figure 5d). The embedding of the DMA-CN probe into the nanofibrous film could be further evidenced by the appearance of the stretching vibrations of C≡N and Ar-N at 2437 and 1358 cm^{-1}, respectively, in the FT-IR spectra (Figure 5e). However, the fluorescence emission of the DMA-CN-embedded nanofibrous film shows a 37 nm blue shift compared with that of the probe solution (Figure 5f). This can be explained as the factor that the amino group in the DMA-CN and the hydroxyl groups in the PVA chain were bound together in the form of hydrogen bonds. This strong intermolecular attraction was verified by the discrete dots in the scatter graph of similar patterns with spikes around the negative sign$(\lambda_2)\rho(-0.035)$, and the δ values are higher than 0.06 obtained by the independent gradient model (IGM) (Figure 5g).

DMA-CN-Embedded Nanofibrous Test Strip for $KMnO_4$ and NaClO Solution Detection. To verify the practical detection capability of the present nanofibrous film, it was placed on a black sponge adhered on a wooden strip for portability and a wide range of applications (Figure 6a). Thus, it can be in direct contact with the suspension solution and present the specific fluorescence response. From the fluorescence images of the test strip for sensing different concentrations of $KMnO_4$, it could be seen that 5 μM $KMnO_4$ could result in a sharp decrease for the intrinsic red

https://doi.org/10.1021/acs.analchem.2c01894
Anal. Chem. 2022, 94, 9184−9192

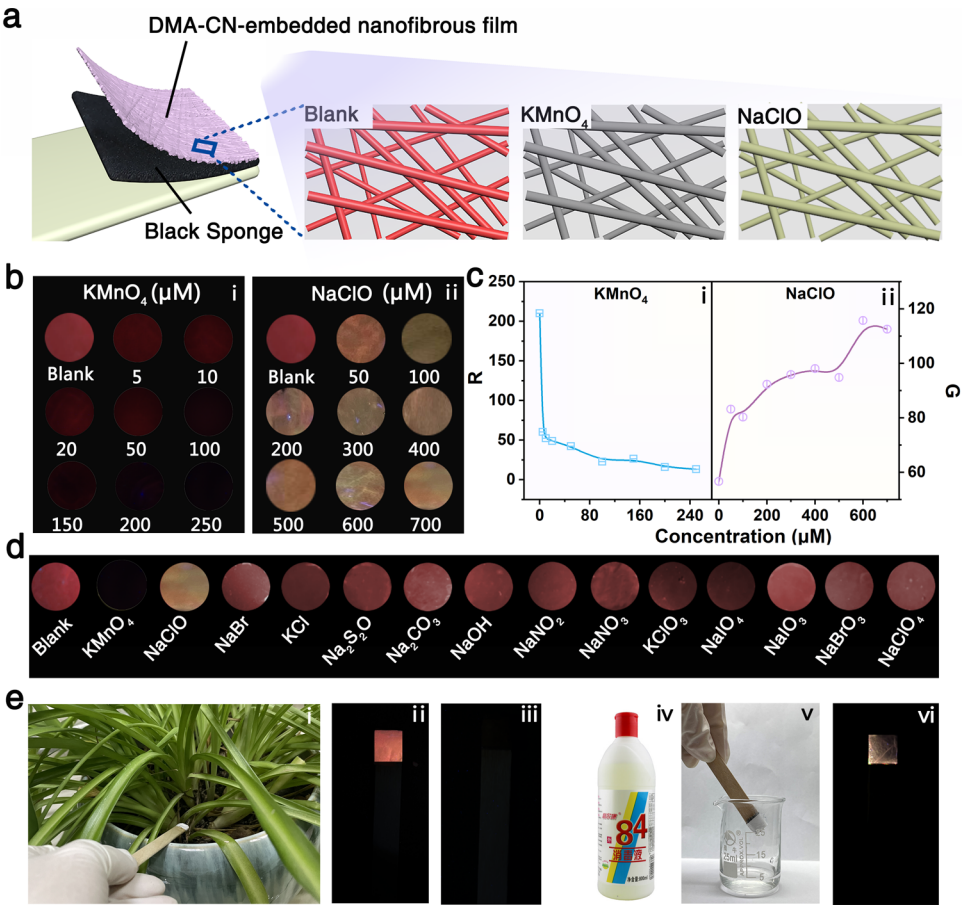

Figure 6. (a) Schematic illustration of the construction of a DMA-CN-embedded nanofibrous test strip and the fluorescence change toward $KMnO_4$ and NaClO; (b) fluorescence images of the test strip before and after detecting (i) $KMnO_4$ (0−250 μM) and (ii) NaClO (0−700 μM); (c) corresponding (i) *R* values and (ii) *G* values of the fluorescent images in (b) as a function of the concentration of $KMnO_4$ and NaClO; (d) fluorescent images of the specificity of the test strip to 12 interferents; and (e) practical fluorescence detection of the test strip for (i−iii) hidden $KMnO_4$ in a pot culture and (iv−vi) 84 disinfectant.

fluorescence emission of the film, and 200 μM $KMnO_4$ can induce a complete fluorescence quenching (Figure 6b-i). For the sensing of NaClO, the red fluorescence is deeply weakened when 50 μM NaClO was added, and then, it changes to pale brown at 100 μM, which is a mixed fluorescence of red and steel blue, followed by no more obvious change trend with higher NaClO concentrations (Figure 6b-ii). The fluorescence change is further analyzed by extracting the average *R* and *G* values of the images and plotting them as a function of the concentration of $KMnO_4$ and NaClO, respectively (Figure 6c). It can be observed that the change trend for detecting $KMnO_4$ is highly consistent with the naked-eye observation, while for NaClO detection, there actually exists an increasing trend of the *G* value, which still shows a concentration-dependent relevance.

The test strip is also proven to hold good specificity in practical tests with negligible influence from the interferents, while the film still maintains the characteristic fluorescence (Figure 6d). The screening for the hidden $KMnO_4$ was demonstrated by spraying a small amount of $KMnO_4$ solution into a pot culture (Figure 6e-i). It can be seen that once the test strip contacts with the topsoil, the characteristic red emission is immediately quenched no matter whether interference from the soil itself and other possible chemical components in soil exists (Figure 6e-ii,e-iii). Another practical test was performed by detecting commercially available 84 disinfectant, of which the main component is NaClO; the characteristic pale-brown emission was immediately observed when the test strip was immersed into 84 disinfectant (Figure 6e-iv−e-vi), demonstrating the promising applicability of the test strip in real industrial risk management.

■ CONCLUSIONS

In summary, a fluorescence−colorimetric dual-mode probe with the D-π-A structure (DMA-CN) was successfully designed, in which dimethylamino as an electron-donating group and TCF as an electron-accepting group were linked by an unsaturated double bond featuring the active site during detection. For the response toward $KMnO_4$, the DMA-CN exhibits purple emission quenching in the fluorescence channel and color changes from blue to yellowish in the colorimetric channel by cutting off the two unsaturated double bonds in the π-conjugation bridge and TCF. In terms of the detection of NaClO, the emission changes from purple to steel blue in the fluorescence channel and the color changes from blue to colorless in the colorimetric channel by limitedly cutting off the π-conjugation bridge linking anilino and TCF. Superior detection performance of the DMA-CN probe toward $KMnO_4$ and NaClO solution was achieved with low fluorescence and colorimetric detection limits ($KMnO_4$: 60 and 91 nM; NaClO: 13.3 and 214 nM), rapid response time (<1 s), and excellent specificity to 12 interferents. The proposed probe design

https://doi.org/10.1021/acs.analchem.2c01894
Anal. Chem. 2022, 94, 9184−9192

strategy has been proven to be reliable for the construction of the DMA-CN-embedded nanofibrous test strip, which is capable for detecting $KMnO_4$ and NaClO with the naked-eye LODs of 5 and 50 μM, respectively. In addition, by tentatively identifying trace $KMnO_4$ solid in pot culture and the NaClO component in 84 disinfectant with the test strip, the applicability of the designed DMA-CN probe was fully verified. We expect that the present probe design would shine light on the efficient probe exploration, and the DMA-CN probe-based sensing strategy would be favorable for a variety of practical applications including environmental monitoring, industrial risk management, public security, human health, etc.

■ ASSOCIATED CONTENT

Supporting Information

The Supporting Information is available free of charge at https://pubs.acs.org/doi/10.1021/acs.analchem.2c01894.

Synthesis of 2-(3-cyano-4,5,5-trimethylfuran-2 (5*H*)-ylidene) malononitrile (TCF) and the probe (DMA-CN), preparation of nanofibrous films, purification of A-CN, purification of A-CO, preparation of the DMA-CN probe solution, preparation of the $KMnO_4$ stock solution, preparation of the NaClO stock solution; preparation of analyte stock solutions, optimization of nanofibrous films, working curve of A-CN, working curve of A-CO, calculation of the percentage of the products (A-CN and A-CO) of DMA-CN toward $KMnO_4$ and DMA-CN-embedded nanofibrous films, preparation of the DMA-CN-embedded test strip, division of the DMA-CN molecule structure for the hole−electron analysis, specificity of DMA-CN toward $KMnO_4$ and NaClO, SEM and contact angle images of the nanofibrous films without DMA-CN, calculated excitation energy, wavelength, and oscillator strength for the low-laying singlet state of DMA-CN, A-CN, and A-CO, and comparison of the recently developed optical methods for the detection of $KMnO_4$ and NaClO (PDF)

■ AUTHOR INFORMATION

Corresponding Authors

Jun Zhang − *Department of Physics Science and Technology, Xinjiang University, Urumqi 830046, China*; Email: zhj@xju.edu.cn

Xincun Dou − *Xinjiang Key Laboratory of Explosives Safety Science, Xinjiang Technical Institute of Physics and Chemistry, Chinese Academy of Sciences, Urumqi 830011, China; Center of Materials Science and Optoelectronics Engineering, University of Chinese Academy of Sciences, Beijing 100049, China;* orcid.org/0000-0001-5825-9937; Email: xcdou@ms.xjb.ac.cn

Authors

Xinyi Yang − *Department of Physics Science and Technology, Xinjiang University, Urumqi 830046, China*

Zhenzhen Cai − *Xinjiang Key Laboratory of Explosives Safety Science, Xinjiang Technical Institute of Physics and Chemistry, Chinese Academy of Sciences, Urumqi 830011, China*

Dezhong Li − *Department of Physics Science and Technology, Xinjiang University, Urumqi 830046, China*

Da Lei − *Xinjiang Key Laboratory of Explosives Safety Science, Xinjiang Technical Institute of Physics and Chemistry, Chinese Academy of Sciences, Urumqi 830011, China*

Yushu Li − *Xinjiang Key Laboratory of Explosives Safety Science, Xinjiang Technical Institute of Physics and Chemistry, Chinese Academy of Sciences, Urumqi 830011, China*

Guangfa Wang − *Xinjiang Key Laboratory of Explosives Safety Science, Xinjiang Technical Institute of Physics and Chemistry, Chinese Academy of Sciences, Urumqi 830011, China*

Complete contact information is available at: https://pubs.acs.org/10.1021/acs.analchem.2c01894

Author Contributions

‖X.Y. and Z.C. contributed equally to this work.

Notes

The authors declare no competing financial interest.

■ ACKNOWLEDGMENTS

We thank the financial supports from the Natural Science Foundation of Xinjiang (2022D01E03), the West Light Foundation of the Chinese Academy of Sciences (CAS Grant No. 2020-XBQNXZ-022), the National Natural Science Foundation of China (22174159, 52172168), Youth Innovation Promotion Association (2022441), the Xinjiang International Science & Technology Cooperation Program (2022E01016), and the Key Research Program of Frontier Sciences (CAS Grant No. ZDBS-LY-JSC029).

■ REFERENCES

(1) Nguyen, V.-N.; Ha, J.; Cho, M.; Li, H.; Swamy, K. M. K.; Yoon, J. *Coord. Chem. Rev.* **2021**, *439*, No. 213936.

(2) Mishra, S.; Singh, A. K. *Coord. Chem. Rev.* **2021**, *445*, No. 214063.

(3) Chu, H.; Yang, L.; Yu, L.; Kim, J.; Zhou, J.; Li, M.; Kim, J. S. *Coord. Chem. Rev.* **2021**, *449*, No. 214208.

(4) Jia, J.; Xu, W.; Yu, Y.; Fu, Y.; He, Q.; Cao, H.; Cheng, J. *Sci. China: Chem.* **2020**, *63*, 116−125.

(5) Ma, C. W.; Ng, K. K. H.; Yam, B. H. C.; Ho, P. L.; Kao, R. Y. T.; Yang, D. *J. Am. Chem. Soc.* **2021**, *143*, 6886−6894.

(6) Ma, Z.; Li, J.; Hu, X.; Cai, Z.; Dou, X. *Adv. Sci.* **2020**, *7*, No. 2002991.

(7) Shen, D.; Jin, W.; Bai, Y.; Huang, Y.; Lyu, H.; Zeng, L.; Wang, M.; Tang, Y.; Wan, W.; Dong, X.; Gao, Z.; Piao, H. L.; Liu, X.; Liu, Y. *Angew. Chem., Int. Ed.* **2021**, *60*, 16067−16076.

(8) Wang, X. F.; Shen, C. Q.; Zhou, C. F.; Bu, Y. Y.; Yan, X. H. *Chem. Eng. J.* **2021**, *417*, No. 129125.

(9) Sarott, R. C.; Viray, A. E. G.; Pfaff, P.; Sadybekov, A.; Rajic, G.; Katritch, V.; Carreira, E. M.; Frank, J. A. *J. Am. Chem. Soc.* **2021**, *143*, 736−743.

(10) Xiao, H.; Zhang, W.; Li, P.; Zhang, W.; Wang, X.; Tang, B. *Angew. Chem., Int. Ed.* **2020**, *59*, 4216−4230.

(11) Tawfik, S. M.; Sharipov, M.; Kakhkhorov, S.; Elmasry, M. R.; Lee, Y.-I. *Adv. Sci.* **2019**, *6*, No. 1801467.

(12) Guo, L. J.; Yang, Z.; Dou, X. C. *Adv. Mater.* **2017**, *29*, No. 1604528.

(13) Chang, X.; Zhou, Z.; Shang, C.; Wang, G.; Wang, Z.; Qi, Y.; Li, Z. Y.; Wang, H.; Cao, L.; Li, X.; Fang, Y.; Stang, P. J. *J. Am. Chem. Soc.* **2019**, *141*, 1757−1765.

(14) Yan, C. X.; Guo, Z. Q.; Chi, W. J.; Fu, W.; Abedi, S. A. A.; Liu, X. G.; Tian, H.; Zhu, W. H. *Nat. Commun.* **2021**, *12*, No. 3869.

(15) Wu, Z.; Fu, X.; Wang, Y. *Sens. Actuators, B* **2017**, *245*, 406−413.

(16) Liu, M.; Zhai, W.; Chen, H.; Zhang, H.; Li, C. *Anal. Chem.* **2020**, *92*, 10792−10799.
(17) Gu, J. P.; Li, X. Q.; Zhou, Z.; Liao, R. S.; Gao, J. W.; Tang, Y. P.; Wang, Q. M. *Chem. Eng. J.* **2019**, *368*, 157−164.
(18) Liu, H.; Zhang, P. S.; Zhang, C. H.; Chen, J.; Jiang, J. H. *Acs Appl. Mater. Interfaces* **2020**, *12*, 45822−45829.
(19) Zhu, B.; Xu, Y.; Liu, W.; Shao, C.; Wu, H.; Jiang, H.; Du, B.; Zhang, X. *Sens. Actuators, B* **2014**, *191*, 473−478.
(20) He, Y.; Miao, L.; Yu, L.; Chen, Q.; Qiao, Y.; Zhang, J.-F.; Zhou, Y. *Dyes Pigm.* **2019**, *168*, 160−165.
(21) Wu, H.; Chen, Y.; Ling, X.; Yuan, W.; Li, B.; Zhou, Z. *J. Mol. Liq.* **2021**, *329*, No. 115465.
(22) Zhou, K.; Bai, H.; Feng, L.; Dai, J.; Cui, M. *Anal. Chem.* **2017**, *89*, 9432−9437.
(23) Chen, J.; Xu, X. X.; Pan, X. X.; Yao, J. Y.; Li, C. G.; Qu, R. J.; Wang, Z. Y. *Chem. Eng. J.* **2018**, *332*, 267−276.
(24) Wu, D.; Chen, L.; Xu, Q.; Chen, X.; Yoon, J. *Acc. Chem. Res.* **2019**, *52*, 2158−2168.
(25) Liu, Y.; Li, J.; Wang, G.; Zu, B.; Dou, X. *Anal. Chem.* **2020**, *92*, 13980−13988.
(26) Shi, G.; Shahid, M. A.; Yousuf, M.; Mahmood, F.; Rasheed, L.; Bielawski, C. W.; Kim, K. S. *Chem. Commun.* **2019**, *55*, 1470−1473.
(27) Wang, B.; Chen, D.; Kambam, S.; Wang, F.; Wang, Y.; Zhang, W.; Yin, J.; Chen, H.; Chen, X. *Dyes Pigm.* **2015**, *120*, 22−29.
(28) Adamo, C.; Barone, V. *J. Chem. Phys.* **1999**, *110*, 6158−6170.
(29) Grimme, S.; Ehrlich, S.; Goerigk, L. *J. Chem. Phys.* **2011**, *32*, 1456−1465.
(30) McLean, A. D.; Chandler, G. S. *J. Chem. Phys.* **1980**, *72*, 5639−5648.
(31) Scalmani, G.; Frisch, M. J.; Mennucci, B.; Tomasi, J.; Cammi, R.; Barone, V. *J. Chem. Phys.* **2006**, *124*, No. 094107.
(32) Jacquemin, D.; Perpe′te, E. A.; Scuseria, G. E.; Ciofini, I.; Adamo, AC. *J. Chem. Theory Comput.* **2008**, *4*, 123−135.
(33) TOMASI, J.; CAMMI, R. *J. Comput. Chem.* **1995**, *16*, 1449−1458.
(34) Frisch, M. J.; Trucks, G. W.; Schlegel, H. B.; Scuseria, G. E.; Robb, M. A.; Cheeseman, J. R.; Scalmani, G.; Barone, V.; Petersson, G. A.; Nakatsuji, H.; Li, X.; Caricato, M.; Marenich, A. V.; Bloino, J.; Janesko, B. G.; Gomperts, R.; Mennucci, B.; Hratchian, H. P.; Ortiz, J. V.; Izmaylov, A. F.; Sonnenberg, J. L.; Williams; Ding, F.; Lipparini, F.; Egidi, F.; Goings, J.; Peng, B.; Petrone, A.; Henderson, T.; Ranasinghe, D.; Zakrzewski, V. G.; Gao, J.; Rega, N.; Zheng, G.; Liang, W.; Hada, M.; Ehara, M.; Toyota, K.; Fukuda, R.; Hasegawa, J.; Ishida, M.; Nakajima, T.; Honda, Y.; Kitao, O.; Nakai, H.; Vreven, T.; Throssell, K.; Montgomery, J. A., Jr.; Peralta, J. E.; Ogliaro, F.; Bearpark, M. J.; Heyd, J. J.; Brothers, E. N.; Kudin, K. N.; Staroverov, V. N.; Keith, T. A.; Kobayashi, R.; Normand, J.; Raghavachari, K.; Rendell, A. P.; Burant, J. C.; Iyengar, S. S.; Tomasi, J.; Cossi, M.; Millam, J. M.; Klene, M.; Adamo, C.; Cammi, R.; Ochterski, J. W.; Martin, R. L.; Morokuma, K.; Farkas, O.; Foresman, J. B.; Fox, D. J. *Gaussian 09*, revision C.01; Wallingford, CT, 2016.
(35) Lefebvre, C.; Rubez, G.; Khartabil, H.; Boisson, J.-C.; Contreras-García, J.; Hénon, E. *Phys. Chem. Chem. Phys.* **2017**, *19*, 17928−17936.
(36) Lu, T.; Chen, F. *J. Comput. Chem.* **2012**, *33*, 580−592.
(37) Humphrey, W.; Dalke, A.; Schulten, K. VMD: Visual m.
(38) Kalinin, A. A.; Smirnov, M. A.; Islamova, L. N.; Fazleeva, G. M.; Vakhonina, T. A.; Levitskaya, A. I.; Fominykh, O. D.; Ivanova, N. V.; Khamatgalimov, A. R.; Nizameev, I. R.; Balakina, M. Y. *Dyes Pigm.* **2017**, *147*, 444−454.
(39) Noirbent, G.; Pigot, C.; Bui, T. T.; Péralta, S.; Nechab, M.; Gigmes, D.; Dumur, F. *Dyes Pigm.* **2021**, *184*, No. 108807.
(40) Kim, S. H.; Lee, S. Y.; Gwon, S. Y.; Son, Y. A.; Bae, J. S. *Dyes Pigm.* **2010**, *84*, 169−175.
(41) Liu, C.; Liu, L.; Li, X.; Shao, C.; Huang, X.; Zhu, B.; Zhang, X. *RSC Adv.* **2014**, *4*, 33507−33513.
(42) Liu, Z.; Lu, T.; Chen, Q. *Carbon* **2020**, *165*, 461−467.
(43) Sjoberg, P.; Jane, S.; Murray, J. S.; Murry, T. B.; Brinck, T.; Politze, Peter. *Can. J. Chem.* **1990**, *68*, 1440−1443.

https://doi.org/10.1021/acs.analchem.2c01894
Anal. Chem. 2022, 94, 9184−9192